

The island dynamics model on parallel quadtree grids

Pouria Mistani ^{a,*}, Arthur Guittet ^a, Daniil Bochkov ^a, Joshua Schneider ^b, Dionisios Margetis ^c, Christian Ratsch ^b, Frederic Gibou ^{a,d}

^a Department of Mechanical Engineering, University of California, Santa Barbara, CA 93106-5070, United States

^b Department of Mathematics and Institute for Pure and Applied Mathematics, UCLA, CA 90095-7121, United States

^c Department of Mathematics, and Institute for Physical Science and Technology, and Center for Scientific Computation and Mathematical Modeling, University of Maryland, College Park, MD 20742, United States

^d Department of Computer Science, University of California, Santa Barbara, CA 93106-5110, United States

ARTICLE INFO

Article history:

Received 21 June 2017

Accepted 31 January 2018

Available online 5 February 2018

Keywords:

Level-set method

Quadtree grids

Epitaxial growth

Ehrlich-Schwoebel barrier

Irreversible aggregation

Robin boundary conditions

ABSTRACT

We introduce an approach for simulating epitaxial growth by use of an island dynamics model on a forest of quadtree grids, and in a parallel environment. To this end, we use a parallel framework introduced in the context of the level-set method. This framework utilizes: discretizations that achieve a second-order accurate level-set method on non-graded adaptive Cartesian grids for solving the associated free boundary value problem for surface diffusion; and an established library for the partitioning of the grid. We consider the cases with: irreversible aggregation, which amounts to applying Dirichlet boundary conditions at the island boundary; and an asymmetric (Ehrlich-Schwoebel) energy barrier for attachment/detachment of atoms at the island boundary, which entails the use of a Robin boundary condition. We provide the scaling analyses performed on the Stampede supercomputer and numerical examples that illustrate the capability of our methodology to efficiently simulate different aspects of epitaxial growth. The combination of adaptivity and parallelism in our approach enables simulations that are several orders of magnitude faster than those reported in the recent literature and, thus, provides a viable framework for the systematic study of mound formation on crystal surfaces.

© 2018 Elsevier Inc. All rights reserved.

1. Introduction

Epitaxial growth is a complex, multiscale process in which a material is deposited on top of another one and takes on the crystalline orientation of the substrate. The growth process results in the formation and evolution of islands and steps [23,38], which accompany the fabrication of many modern opto-electronic devices below the roughening transition. Hence, epitaxial growth is of fundamental technological importance. Notable examples of related devices include transistors in microelectronics, quantum dots for photonic-crystal lasers, quantum dot-based enhancements in the energy sector, and devices for nonvolatile storage which is sought to replace hard drives, flash and RAM memories. Other applications of epitaxial growth include catalysts, which are used, e.g., in the energy sector, food processing, and environmental science.

In this paper, we introduce a computational approach for the simulation of island evolution in large epitaxial systems. Our main motivation is the need to make accurate predictions for the formation of crystal surface features, e.g. mounds, at large scales. We start with the island dynamics model (IDM) by Caflisch et al. [8,40]. This description relies on the for-

* Corresponding author.

E-mail address: pouria@umail.ucsb.edu (P. Mistani).

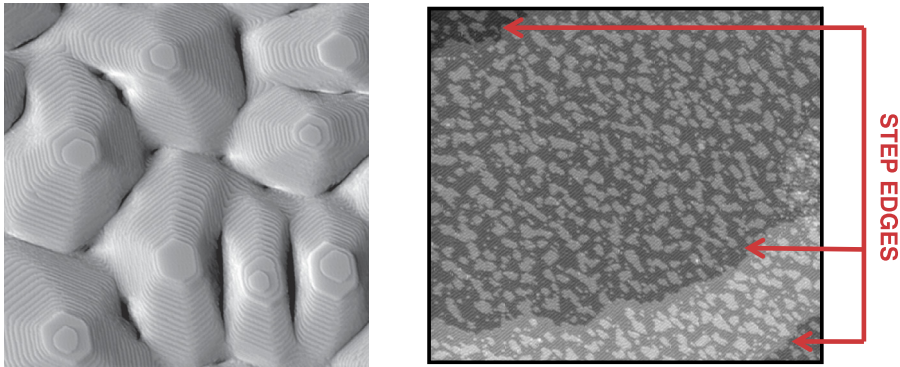


Fig. 1. Single-Tunneling-Microscope (STM) images of epitaxially grown thin films where macroscopic or mesoscale features may develop, e.g., mounds (left image from [24]) and step edges (right image from [4]).

mulation of a free boundary value problem, in the spirit of the Burton–Cabrera–Frank (BCF) theory [7]. The model has the following main elements: (i) a diffusion-type equation for the density of adsorbed atoms (adatoms) in the region (terrace) between successive steps, which includes nucleation in a mean-field sense; (ii) Dirichlet or Robin boundary conditions for the adatom density at the island boundaries; and (iii) a kinetic law for the normal velocity of each boundary by mass conservation. We numerically solve this system on a forest of quadtree grids, and in a parallel environment by using the framework introduced in the context of the level-set method by Mirzadeh et al. [32]. This framework utilizes the discretizations of Min and Gibou [30] for the associated free boundary value problem, and the `p4est` library of Burstedde et al. [6] for the partitioning of the grid. We apply our approach to the growth of mounds in *homoepitaxy*, where the deposited material is the same as the substrate.

From a physical viewpoint, basic processes that occur during epitaxial growth include the nucleation, growth, and coalescence of two-dimensional islands. Close to thermodynamic equilibrium, homoepitaxial growth proceeds atomic layer by atomic layer. However, growth is far from equilibrium for many homoepitaxial systems, and, therefore, the observed surface morphology is a result of kinetic limitations. In particular, multilayer growth may become unstable and, hence, mounds may form. This phenomenon has been observed experimentally for many epitaxial systems such as surfaces of Cu [17,55], Fe [47], Ag [53] or Pt [5].

The microscopic process that usually underlies mound formation is an additional (Ehrlich–Schwoebel, ES) energy barrier characterizing the attachment/detachment of atoms at island boundaries or edges of steps [16,44]. For some applications, these mounds can seriously degrade the performance of the device being grown; for example, in the case of metallic films the electric connections between layers can be hampered [49]. In contrast, in some other cases these mounds can be regarded as almost zero-dimensional defects with novel properties that can be exploited in the laboratory setting [54]. An example of such mounds which form for growth of Pt on Pt(111) is shown in Fig. 1 [left panel]. In the suitable kinetic regime of these systems, step edges with interesting dynamics are evident (see Fig. 1 [right panel]).

Hence, the understanding and control of crystal surface instabilities that lead to mound formation are significant goals in materials science. Accordingly, the development of computational methods that accurately and efficiently describe the growth of thin films has been the focus of intensive research [25,1,28,9]. Computational challenges in this direction are primarily due to the multiscale nature of epitaxial growth: On the one hand, growth of islands and the flow of steps is determined by the diffusion (and attachment) of individual adatoms, which sets time and length scales of the order of 10^{-6} sec and Ångstroms. On the other hand, typical devices can be microns in lateral size (and hundreds of layers thick), and are grown at timescales that are seconds or minutes.

To develop a computational approach faithful to the multiscale character of epitaxial growth, we use the IDM and a level-set method for its simulation [8,14,39,33,20,52,40]. The model has the mesoscale features of the BCF theory for steps [7], namely, coarse-graining of the atomistic dynamics in the lateral (parallel to a fixed reference plane) directions and retention of atomistic detail in the growth direction; thus, the model is particularly well-suited for simulating epitaxial growth. Yet, this model has so far only used uniform grids on sequential machines.

In the present paper, we overcome this limitation via an approach that uses adaptive mesh refinement techniques and parallel strategies to significantly increase the size of systems that can be considered, as well as to offer a significant simulation speedup. To validate our computational approach, we carry out a series of numerical experiments associated with mound formation. In these examples, we invoke irreversible aggregation, which corresponds to a Dirichlet condition in the IDM; and an ES barrier which is modeled through a Robin condition at the step edge.

Section 2 provides an overview of the IDM (Section 2.1), and describes the multi-level-set representation for the motion of island boundaries (Section 2.2). Section 3 details the parallel strategy and the discretization algorithms for the simulation of multi-layer growth and dynamics of step edges. In Section 4 we present numerical examples that serve the validation of our computational approach. Section 5 concludes our paper with a summary of our framework and an outline of related, open problems.

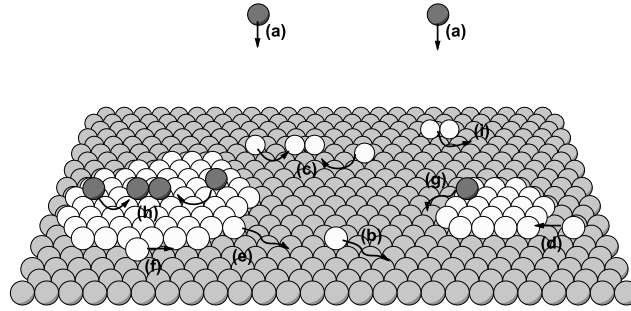


Fig. 2. Schematic of atomistic processes during epitaxial growth. Atoms are deposited onto the surface [(a)]; diffuse on the surface with atomistic (hopping) rate D [(b)]; attach to [(d)], or detach from [(e)] an island boundary or a step edge; or diffuse along an island edge [(f)]. In addition to these processes, two atoms may coalesce and form a dimer [(c), (h)], which might be stable and grow, or break up [(i)].

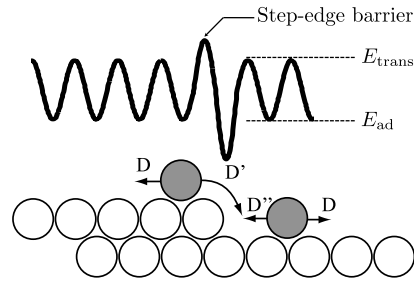


Fig. 3. Schematic of an asymmetric (ES) step-edge barrier. The lower panel shows the atomistic configuration of a step edge, to which an adatom attaches with rate D' (D'') from the upper (lower) terrace. The upper panel depicts the corresponding energy landscape in one spatial coordinate.

2. Island dynamics model and multi-level-set representation

In this section, we review the basic elements of the IDM, which forms an extension of the BCF theory [7]; see also [15, 23]. Furthermore, we describe a level-set approach that simultaneously keeps track of the motion of many island boundaries.

2.1. Island dynamics model

The IDM [8,14,39,33,20,52,40] treats the evolution of islands and steps as a free boundary problem: each boundary moves by mass conservation, in the spirit of the BCF model [7]. Island boundaries and step edges have an atomic height, a , thus retaining the lattice discreteness in the vertical direction. In contrast, the diffusion of adatoms on each terrace is considered as a continuous process by coarse-graining of the atom hopping. Hence, adatom diffusion is studied via the dynamics of the adatom density, $\rho(\mathbf{x}, t)$, a continuous variable.

Specifically, $\rho(\mathbf{x}, t)$ evolves through the equation

$$\frac{\partial \rho}{\partial t} = F + \nabla \cdot (\mathcal{D} \nabla \rho) - 2 \frac{dN}{dt}, \quad (1)$$

which accounts for adatom diffusion with diffusivity $\mathcal{D} = Da^2$ (where D is the hopping rate), external material deposition with flux F , and nucleation of islands with rate dN/dt where $N(t)$ is the island density (see Fig. 2). In the following analysis, we set the lattice spacing, a , or step height, equal to unity, $a = 1$; thus, we replace \mathcal{D} by D .

By use of a mean-field approximation, the nucleation rate dN/dt is defined by

$$\frac{dN}{dt} = \sigma_1 D \langle \rho^2(\mathbf{x}) \rangle, \quad (2)$$

where σ_1 is a capture number [2,19] and $\langle \cdot \rangle$ denotes the average taken over all lattice sites. Note that the capture number, σ_1 , is a phenomenological, effective parameter that expresses how effectively an island of given size in a given environment (i.e., with a given capture area) competes for the available monomers on the crystal surface [2]. Stochastic elements for island nucleation have been added to the IDM, and validated by comparison to an (atomistic) kinetic Monte Carlo (KMC) model [39].

A few additional comments on (2) are in order. This equation dictates when the adatom density is large enough to seed a new island. The location of nucleation takes into account the stochasticity inherent to atomistic dynamics, as described in [39]. From a computational/algorithmic perspective, this description of nucleation can be split into the following stages:

1. Compute ρ^2 at each grid point (label them $i = 1, \dots, n$), weighted by its surrounding computational cell area $w(\mathbf{x}_k)$.
2. Compute the sum over all these values, keeping partial sums $Q_k = \sum_{i=1}^k w(\mathbf{x}_k) \times \rho^2(\mathbf{x}_k)$.
3. Generate a random number, r in $[0, Q_n]$.
4. Find the first index k such that $r \geq Q_k$.
5. Seed a circular island of size $2 \Delta x$ at \mathbf{x}_k .

The diffusion equation (1) for the adatom density, ρ , must be supplemented with boundary conditions at island boundaries or step edges. The boundary conditions for ρ reflect important atomistic processes and, thus, have a crucial impact on the ability of the IDM to make physical predictions. In general, a Robin condition for ρ at the island boundary has been extensively invoked in epitaxial systems [15,50,23]. In regard to the upper terrace (see Fig. 3), this condition assumes the form

$$\nabla \rho \cdot \mathbf{n} + \frac{D'}{D - D'} \rho = \frac{D'}{D - D'} \rho_{\text{eq}}, \quad (3)$$

where ρ and $\nabla \rho$ are restricted to the island boundary, the atomistic rate D' expresses the energy barrier for adatom diffusion over a step edge or island boundary, ρ_{eq} is an equilibrium adatom density, and \mathbf{n} is the outward normal to the island boundary.

Boundary condition (3) describes the effect of the ES barrier (for $D' \neq D$), and has been formally derived from atomistic dynamics [27]. Note that an ES barrier causes any atom located next to the step edge to be more likely to diffuse to the adjacent site on the same terrace (with rate D) than diffuse downwards (with rate D'). Similarly, an additional energy barrier, expressed by rate D'' , may be present on the lower terrace (see Fig. 2 [right panel]). Physically, this additional step-edge barrier causes an uphill current and the formation of mounds, as shown both by continuum models [50] and KMC simulations [51].

As $D' \rightarrow D$, equation (3) reduces to the Dirichlet condition $\rho(\mathbf{x}) = \rho_{\text{eq}}$ [7,38,27]. Notably, in [10], an expression for ρ_{eq} is derived with no step-edge (ES) barrier; while in [35], the authors derive and implement an expression for ρ_{eq} under a step-edge barrier. In principle, this ρ_{eq} depends on the microscopic rates for detachment and edge diffusion [8].

Equations (1)–(3) need to be complemented with a velocity law for the motion of the free boundary. Specifically, the normal velocity field, \mathbf{v} , that characterizes the motion of the island boundary is computed by adatom mass conservation according to the equation

$$\mathbf{v} = \left(D^- \frac{\partial \rho^-}{\partial \mathbf{n}} - D^+ \frac{\partial \rho^+}{\partial \mathbf{n}} \right) \mathbf{n}, \quad (4)$$

which accounts for the total mass flux toward the boundary from the upper (+) and lower (−) terrace. This equation can be enriched with a term that expresses step-edge diffusion [37]. This extension lies beyond our present scope. Equations (1)–(4) form the core of the IDM.

2.2. Multi level-set representation of island dynamics

Next, we describe a multi-level-set representation of the IDM that is best suited to our main purpose of simulating the evolution of large epitaxial systems in this paper. The desired representation exploits the free-boundary approach inherent to the IDM (Section 2.1), as explained below.

First, we emphasize that the IDM is numerically resolved by use of the level-set method, introduced in [34], to keep track of the motion of the island boundaries. The level-set method represents an arbitrary contour as $\Gamma = \{\mathbf{x} \in \mathbb{R}^n \mid \phi(\mathbf{x}) = 0\}$, where $\phi(\mathbf{x})$ is a Lipschitz continuous function. The region enclosed in Γ and the region outside Γ are defined as $\{\mathbf{x} \in \mathbb{R}^n \mid \phi(\mathbf{x}) < 0\}$ and $\{\mathbf{x} \in \mathbb{R}^n \mid \phi(\mathbf{x}) > 0\}$, respectively. In the IDM described in [8,14,40], the boundary of islands of height l is described as $\Gamma_l = \{\mathbf{x} : \phi(\mathbf{x}) = l\}$. In the present work, the boundary of islands of height l is described by the zero level-set of a level-set function ϕ_l as depicted in Fig. 4, i.e. we use as many level-set functions as the number of atomic layers, with each level-set function ϕ_l “recycled” when it represents a complete layer.

The rationale for applying this formalism and, thus, for choosing not to represent all the layers with a single level-set function, can be outlined as follows: (i) Our choice enables the reinitialization of the level-set functions, which in turn increases mass conservation [48,41,30]; and (ii) the motion of the boundaries at different islands’ height can be processed independently, which increases computational efficiency. Specifically, in this multi-level-set framework, the region occupied by the island of height l is defined as $\Omega_l = \{\mathbf{x} \mid \phi_l(\mathbf{x}) > 0 \text{ and } \phi_{l-1}(\mathbf{x}) < 0\}$. If an island is the top most, then $\Omega_l = \{\mathbf{x} \mid \phi_{l-1}(\mathbf{x}) < 0\}$. The substrate is defined as $\Omega_0 = \{\mathbf{x} \mid \phi_0(\mathbf{x}) > 0\}$.

In this vein, the variable ρ_l describes the adatom density on islands of height l (see Fig. 4). Accordingly, boundary conditions for ρ_l in the form of (3) are imposed on the set where $\phi_l = 0$ and also $\phi_{l-1} = 0$ if $l > 0$. Once the velocity field \mathbf{v}_l describing the dynamics of the islands of height l is computed, ϕ_l evolves according to the equation

$$\frac{\partial \phi_l}{\partial t} + \mathbf{v}_l \cdot \nabla \phi_l = 0; \quad (5)$$

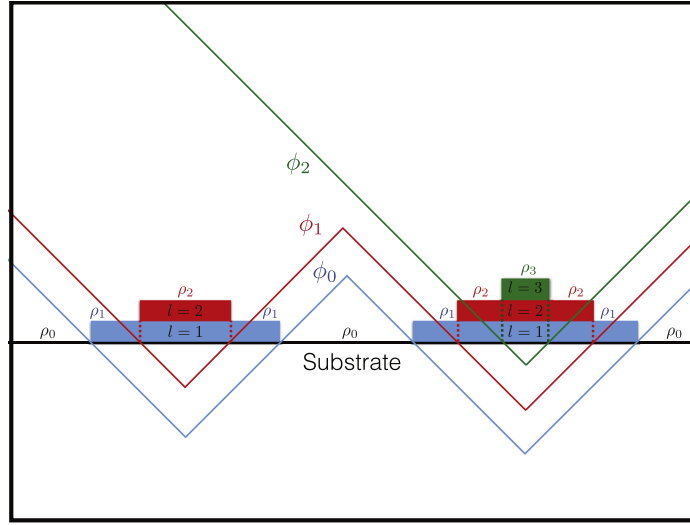


Fig. 4. Level-set representation of the IDM in the present framework. The zero-level set of ϕ_l represents the boundary of islands of height l onto which the adatom density is described by ρ_l .

cf. step velocity law (4). In order to transform an arbitrary level-set function ϕ_l^0 into a signed distance function ϕ_l , we solve the reinitialization equation [48]

$$\frac{\partial \phi_l}{\partial \tau} + \text{sign}(\phi_l^0) (|\nabla \phi_l| - 1) = 0, \quad (6)$$

where τ is a fictitious time and `sign` refers to the signum function.

3. Parallel strategy on adaptive quadtree grids

The numerical implementation of the IDM has so far only considered uniform grids. This approach causes limitations in applications to systems with many islands and steps. Specifically, in the case where one aims to simulate multi-layer growth or examine the dynamics of step edges, uniform grids are limited in their ability to consider large systems because of memory constraints and/or slow speed of simulations. In this section, we introduce a parallel strategy on adaptive grids that enables efficient simulations of the IDM and resolve island dynamics in large epitaxial systems. This strategy makes use of recent computational advances in adaptive mesh refinement.

We add a few comments on these advances. In particular, Chen et al. [12] introduced discretizations for solving the diffusion equation in irregular domains by using Quadtree grids. Min and Gibou [30] introduced discretizations on Quadtree grids for free boundary problems using the level-set method. These two approaches were combined to solve the Stefan problem in [13]. Using this framework and the work of Papac et al. [35] (see also [21]), Papac et al. [36] derived a scheme to solve the Stefan problem with Robin boundary conditions on Quadtree grids and briefly considered the application of this scheme to the IDM. In [32], Mirzadeh et al. developed the level-set technology on Quadtree/Octree grids in the context of distributed computations using the discretizations of Min and Gibou [30] and the p4est library of Burstedde et al. [6].

In the remainder of this section, we will describe the computational framework (sections 3.1–3.3) and how it can be used for the two cases where we have a Dirichlet boundary condition (which corresponds to the case without a step-edge barrier); and when we have a Robin boundary condition, which is needed when a step-edge barrier is present (sections 3.4–3.6).

3.1. Quadtree data structure and refinement criterion

Quadtrees are standard data structures that have been first introduced in the context of computer graphics. The interested reader is referred to the excellent books by Samet for more details [42,43]. Referring to Fig. 5, we associate the entire computational cell with the root of a quadtree structure. Subsequently, cells are recursively split into four children of equal size according to a refinement criterion and until the limits set for the smallest and largest cells are reached. We define the level of the root cell to be 0 and increment it by 1 for its children. In particular, we will call a (l_{\min}, l_{\max}) -grid, an adaptive grid sampling a computational domain of size $L \times L$ for which the smallest cells have size $L \times 2^{-l_{\max}}$ and the largest cells have size $L \times 2^{-l_{\min}}$.

The two main equations of the IDM are parabolic equation (1), which describes the evolution of the adatom density, ρ , and level-set equations (5) and (6) which are used to represent the evolution of the island boundaries. In both cases, the information near the island boundaries is what drives the accuracy of the simulation. Indeed, the diffusion equation for the adatom density, ρ , is a parabolic equation and therefore produces smooth solutions in the entire domain, except

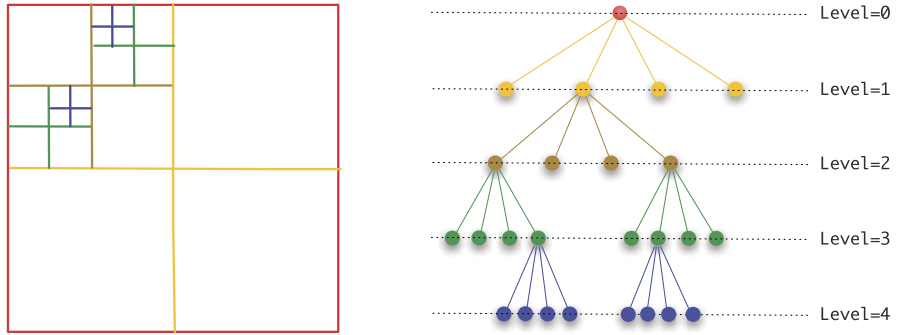


Fig. 5. Discretization of a two-dimensional domain (left) and its quadtree representation (right). The entire domain corresponds to the root of the tree (level 0). Each cell can then be recursively subdivided further into four children. In this example, the tree is non-graded, since the difference of level between some adjacent cells exceeds one. (For interpretation of the colors in figures, the reader is referred to the web version of this article.)

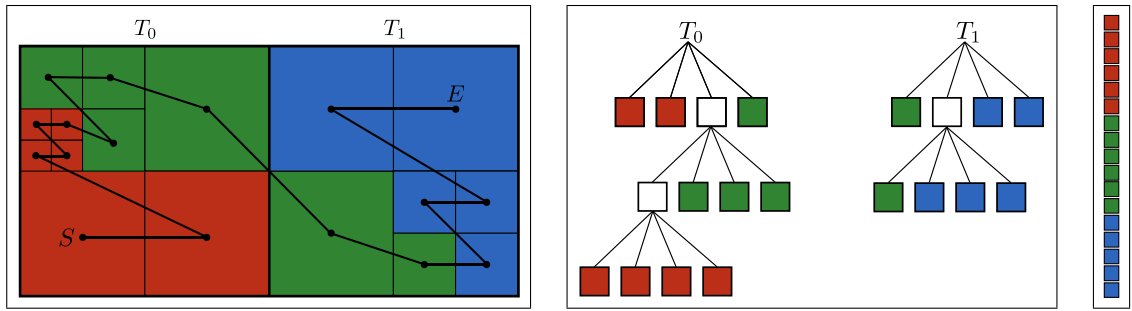


Fig. 6. Two trees, T_0 and T_1 , constitute the ‘forest’. The Z-ordering (left) of the Quadtree’s leaves (center) is used to partition the data among the available processes (right). In this figure, the different colors correspond to different processor ranks. S represents the starting cell and E the last cell visited. In the p4est library, only the one-dimension array (right) is stored among the available processes.

near the boundary of each island. Specifically, boundary conditions applied on each side of the island boundary (upper and lower terraces) produce discontinuous solutions, ρ , and/or its gradient. Likewise, the evolution of the level-set functions ϕ_l is directly linked to the resolution near the island boundaries or step edges [30].

Hence, we use a refinement criterion that automatically sets the finest resolution near the zero-level set of each ϕ_l , i.e. we split a computational cell \mathcal{C} if

$$\min_{v \in \text{vertices}(\mathcal{C})} |\phi_l(v)| \leq \text{Lip}(\phi_l) \cdot \text{diag-size}(\mathcal{C}), \quad (7)$$

where $\text{diag-size}(\mathcal{C})$ refers to the length of the diagonal of \mathcal{C} and v refers to its vertex. Likewise, we merge with its parent cell, any cell \mathcal{C} for which the following condition holds:

$$\min_{v \in \text{vertices}(\mathcal{C})} |\phi(v)| > \text{Lip}(\phi) \cdot \text{diag-size}(\mathcal{C}). \quad (8)$$

The ‘parameter’ $\text{Lip}(\phi)$ in equations (7) and (8) controls how drastic the size difference between adjacent cells can be. In the present work, we take a value of $\text{Lip}(\phi) \approx 1.1$ to generate the grids depicted in Section 4.

3.2. Parallel framework

Next, we outline the main idea of the parallelism in our approach. The parallel framework that we use is the one introduced by Mirzadeh et al. [32]. This framework employs the p4est library for the partitioning of the grid and an algorithm that constructs local trees that enable the discretizations detailed in Sections 3.4 and 3.5. Additional parallel algorithms are constructed to number the islands on the surface in order to compute important statistics, as described in Section 3.3.

When considering parallel computation, where the communication of data between processes is orders of magnitude more time consuming than the computation itself, the main focus of algorithm design is to reduce the number of computations and/or hide the cost of communication by intertwining them with computation. Reducing communication is achieved by grouping, or partitioning, the data in the local memory of each process. The strategy of Burstedde et al. [6] is illustrated in Fig. 6: (1) a macromesh of uniform cells is created and replicated on each process; (2) a forest of Quadtrees is created

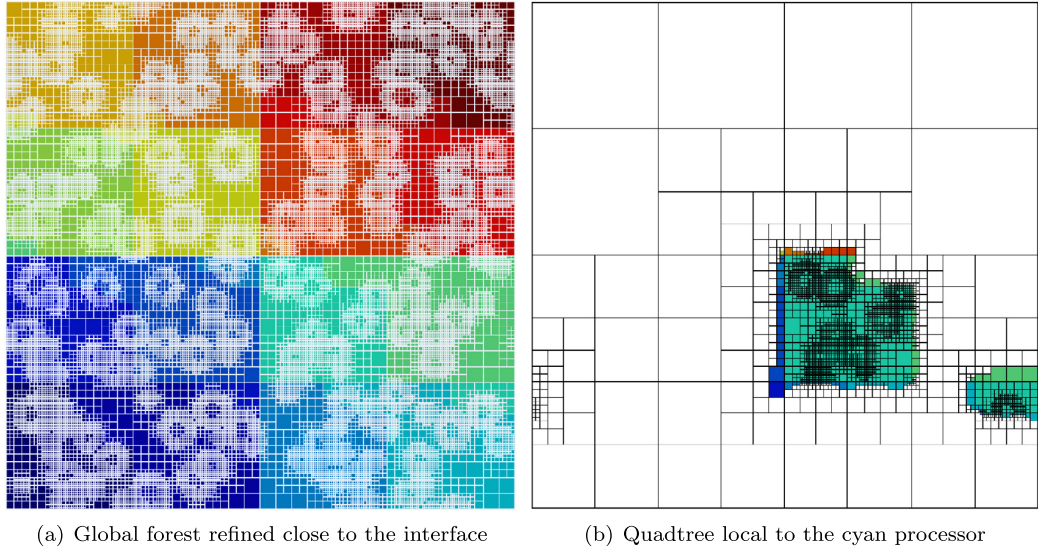


Fig. 7. Left: an example of a computational grid partitioned among 16 processes (color-coded) and the global forest refined close to the interface. Right: the local tree to one process refined to match local islands. Note the surrounding ghost layer from neighboring processes with different colors.

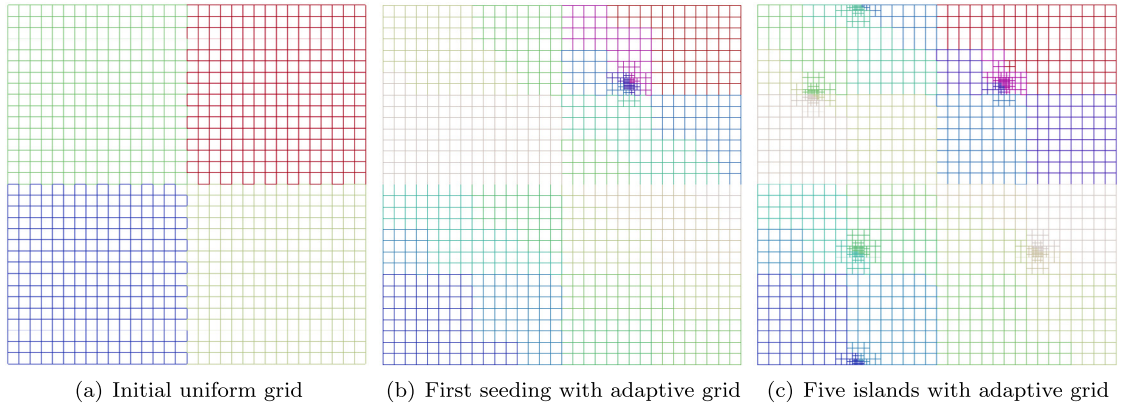


Fig. 8. Example of adaptive grids and partitioning at different computational times. Processors' rank are in color.

recursively using all processes and partitioned among them. The partitioning uses a Z-ordering of the Quadtree leaves, which are recorded in a one-dimensional array before being split equally among the available processes. The application of the Z-ordering clusters the data contiguously, as depicted in Fig. 6, and thus subsequently minimizes the amount of communication during the discretization phase.

Since the p4est library only stores the one-dimensional array of the forest's leaves, an algorithm for constructing the local Quadtree on each process is used in order to apply the discretizations described below. The procedure introduced by Mirzadeh et al. [32] is to create a local tree in such a way that the levels of its leaves correspond to that of the one-dimensional array locally. Globally, the available processes represent the global grid but only store their local portion plus data at points surrounding each processor, i.e. ghost layer, that is necessary to discretize the equations. The result of this process is illustrated in Fig. 7. The adaptivity of the Quadtree to the formation of new islands is illustrated in Fig. 8; it is refined close to the islands and coarsens elsewhere according to the refinement criteria.

3.3. Numbering the islands

We now introduce an algorithm to compute the number of islands for a given level. This task is non-trivial because the islands can span multiple processes, as depicted in Fig. 9.

The first step of our algorithm is for each process to number its local islands, with an offset. For the purpose of demonstration, we choose an offset equal to 10 (we choose an offset of 10^6 in practice), so that the islands of process p can be numbered from $10p$ to $10(p + 1) - 1$. In practice, any number greater than the maximum number of islands that a single process can have is suitable. The local island numbering is carried out by going through the local nodes. Such that for each

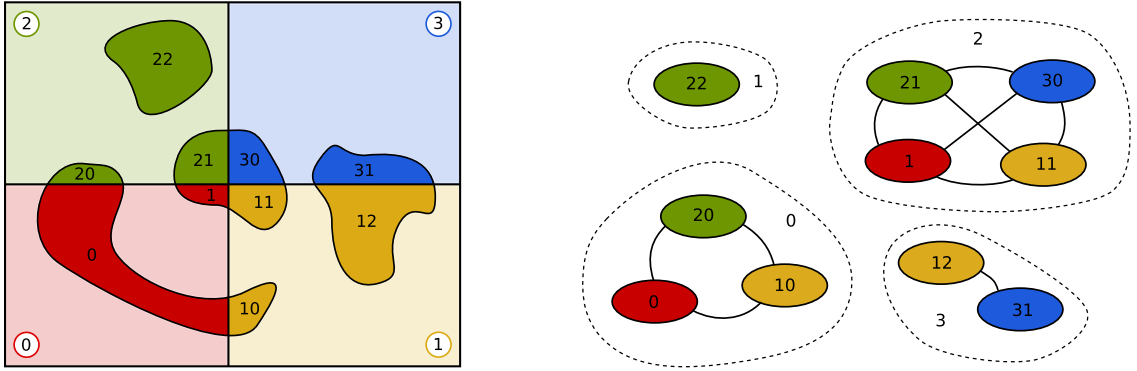


Fig. 9. Left: Four islands spread across four processes. Each process p has assigned a number to its local islands, with an offset equal to $10p$. Right: the global graph connecting the local islands. Each component of this graph is a unique global island.

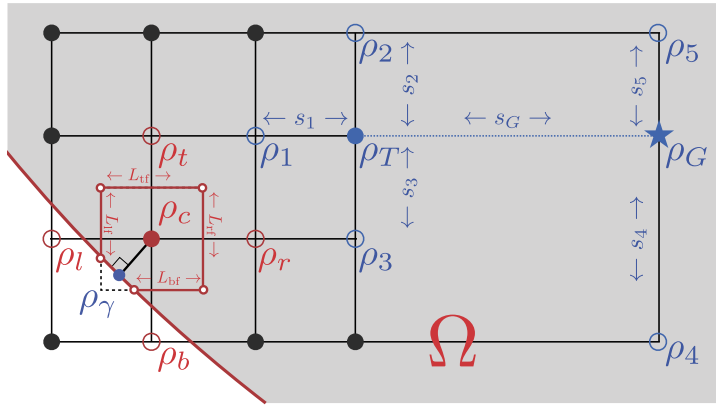


Fig. 10. Stencils used in the discretization of the adatom density. We use a finite volume approach for nodes that are adjacent to the islands' boundary Γ (where the grid is locally uniform) and a finite difference approach for the other nodes.

non-numbered node with $\phi_l < 0$, assigning a number to it and recursively assigning the same number to all the neighboring nodes that are part of the same island, i.e. that also have a negative ϕ_l value.

The next step is to construct a graph where each node represents a local island and two nodes are connected if the local islands are connected through the ghost layer that connects two processes. In order to build this graph, we must first communicate the number of local islands for each process and the island numbers of the points in the ghost layer. With this information, each process can build a graph containing all the global nodes and with the edges involving its local islands.

Finally, we gather the graph across all the processes, thus providing each process with the global graph connecting all the local islands across all the processes. Each process can then count the number of connected components of the graph and assign a unique global number to each component, which is the global island number.

3.4. Solving for the adatom density

The adatom density ρ_l has to be solved on the corresponding terrace Ω_l with appropriate boundary conditions applied on the boundary of the terrace. By (1), on an island of height l , the adatom density satisfies the equation

$$\frac{\partial \rho_l}{\partial t} = F + \nabla \cdot (D \nabla \rho_l) - 2 \frac{dN}{dt}.$$

To solve this equation, we use a Crank–Nicholson scheme in time, writing

$$\frac{\rho^{n+1} - \rho^n}{\Delta t} = F + \frac{1}{2} \nabla \cdot (D \nabla \rho^{n+1}) + \frac{1}{2} \nabla \cdot (D \nabla \rho^n) - 2 \frac{dN}{dt}, \quad (9)$$

where we have omitted the subscript l (i.e. $\rho = \rho_l$ in this section) and $\frac{dN}{dt} = \sigma_1 D(\rho^2(\mathbf{x}))$ is taken at time $t = t^n$; cf. (2). The discretizations of the terms of the form $\nabla \cdot (D \nabla \rho)$ depend on whether we consider a grid node adjacent to the interface or not, as illustrated in Fig. 10.

3.4.1. Discretization far from the island boundaries

The difficulty in discretizing $\nabla \cdot (D \nabla \rho)$ at a grid node that is not near the island boundary comes from the potential presence of a T-junction configuration, i.e. the case where one grid node is missing in one of the Cartesian directions. In that case, Min et al. [31] derive a third-order accurate definition of a ghost value, ρ_G :

$$\rho_G = \frac{\rho_4 s_5 + \rho_4 s_4}{s_4 + s_5} - \frac{s_4 s_5}{s_2 + s_3} \left(\frac{\rho_2 - \rho_0}{s_2} + \frac{\rho_3 - \rho_0}{s_3} \right),$$

where s_i is the size of the segments depicted in Fig. 10. This definition provides a way to discretize the Poisson operator, at the grid node T , as

$$\nabla \cdot (D \nabla \rho)_T = \frac{2}{s_G + s_1} \left(\frac{\rho_G - \rho_T}{s_G} - \frac{\rho_T - \rho_1}{s_1} \right).$$

From this definition, we fill the corresponding row of the linear system for the grid node T .

3.4.2. Discretization near the island boundaries

For grid nodes that are adjacent to the interface, the discretization must account for the boundary condition given by equation (3). Following Papac et al. [35], we consider the integration of the time discretization (9) in the dual cell \mathcal{C} centered at the local grid node c (see Fig. 10), viz.,

$$\int_{\mathcal{C} \cap \Omega} \rho^{n+1} - \frac{\Delta t}{2} \nabla \cdot (D \nabla \rho^{n+1}) d\Omega = \int_{\mathcal{C} \cap \Omega} \rho^n + \frac{\Delta t}{2} \nabla \cdot (D \nabla \rho^n) + \Delta t F - 2 \Delta t \frac{dN}{dt} d\Omega,$$

where Ω is the domain defined by the island of height l . By applying the divergence theorem on the diffusion terms, we obtain

$$\begin{aligned} \int_{\mathcal{C} \cap \Omega} \rho^{n+1} d\Omega - \frac{D \Delta t}{2} \int_{\partial(\mathcal{C} \cap \Omega)} \nabla \rho^{n+1} \cdot \mathbf{n} d\Gamma &= \int_{\mathcal{C} \cap \Omega} \rho^n + \Delta t \left(F - 2 \frac{dN}{dt} \right) d\Omega \\ &\quad + \frac{D \Delta t}{2} \int_{\partial(\mathcal{C} \cap \Omega)} \nabla \rho^n \cdot \mathbf{n} d\Gamma, \end{aligned}$$

where $\partial(\mathcal{C} \cap \Omega)$ refers to the boundary of $(\mathcal{C} \cap \Omega)$, i.e. the part of the computational cell that belongs to the island of height l . The boundary integrals are further split into two parts: the boundary of the computational cell \mathcal{C} that belongs to the island of height l and the part of the island boundary that is located in \mathcal{C} :

$$\int_{\partial(\mathcal{C} \cap \Omega)} \nabla \rho^{n+1} \cdot \mathbf{n} d\Gamma = \int_{\partial \mathcal{C} \cap \Omega} \nabla \rho^{n+1} \cdot \mathbf{n} d\Gamma + \int_{\mathcal{C} \cap \partial \Omega} \left(\frac{D'}{D - D'} \rho_{eq} - \frac{D'}{D - D'} \rho \right) d\Gamma. \quad (10)$$

In the above equation, we invoked Robin boundary condition (3) in the last term.

Next, we discuss the computation of the integrals on the right-hand side of (10). The integral of the unknown function ρ over the boundary $\mathcal{C} \cap \partial \Omega$ is approximated by the value of ρ at the point γ on the boundary (see Fig. 10) multiplied by the length of the boundary $\mathcal{C} \cap \partial \Omega$, i.e.

$$\int_{\mathcal{C} \cap \partial \Omega} \rho d\Gamma \approx \rho_\gamma \int_{\mathcal{C} \cap \partial \Omega} d\Gamma.$$

The point γ is defined as the intersection of the boundary and a straight line orthogonal to the boundary at γ and passing through the grid point c under consideration. At γ , the adatom density satisfies the Robin boundary condition (3). Moreover, ρ_c and ρ_γ are related through a Taylor expansion for ρ at γ in the normal direction as

$$\rho_c = \rho_\gamma - d \frac{\partial \rho}{\partial \mathbf{n}} + \mathcal{O}(d^2) \quad (11)$$

where d is the signed distance between the grid point c and point γ . Combining (3) and (11) we get the following estimation for ρ_γ

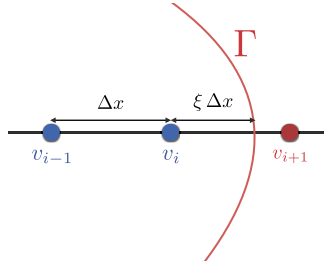


Fig. 11. Boundary condition for irreversible aggregation. The grid nodes on each side of the island boundary, Γ , belong to different islands' height.

$$\rho_Y = d \frac{\rho_c + d \frac{D'}{D - D'} \rho_{eq}}{1 + d \frac{D'}{D - D'}}.$$

Furthermore, we approximate the first integral on the right-hand side of (10) as (see Fig. 10)

$$\int_{\partial C \cap \Omega} \nabla \rho^{n+1} \cdot \mathbf{n} d\Gamma = \frac{\rho_r - \rho_c}{s_r} L_{rf} - \frac{\rho_c - \rho_l}{s_r} L_{lf} + \frac{\rho_t - \rho_c}{s_r} L_{tf} - \frac{\rho_c - \rho_b}{s_r} L_{bf},$$

where L_{rf} (L_{lf} , L_{tf} and L_{bf} , respectively) is the length fraction of the right (left, top and bottom, respectively) face that is in Ω . Finally, we approximate the integral of a quantity Q over $C \cap \Omega$ as

$$\int_{C \cap \Omega} Q d\Omega = Q_c \int_{C \cap \Omega} d\Omega,$$

where Q_c denotes the value of Q at the center of cell C . The integrations are performed by the algorithms introduced in [29]. These approximations define the coefficients in the linear system associated with grid node c .

3.4.3. Case with irreversible aggregation

Irreversible aggregation is the regime in which $D' \rightarrow D$, i.e. when the Robin condition (3) reduces to the Dirichlet condition $\rho(\mathbf{x}) = 0$, taking $\rho_{eq} = 0$. This case deserves special attention: Numerically, the method described in Section 3.4.2 is prone to numerical errors in this case. To address this particular situation, we directly impose the condition $\rho(\mathbf{x}) = \rho_{eq}$ of Chen et al. [11], which is based on the Ghost-Fluid approach of Gibou et al. [18] and the Shortley–Wheller technique [45]. The discretization of the operator $\nabla \cdot (D \nabla \rho)$ in equation (1) follows a dimension-by-dimension approach, i.e. one treats the x -component of $\nabla \cdot (D \nabla \rho)$ with the Dirichlet condition in the x -direction only: The discretization in the x -direction at the grid node v_i is given by the scheme (see Fig. 11)

$$\frac{\partial}{\partial x} \left(D \frac{\partial \rho}{\partial x} \right) (v_i) \approx \frac{D_{i+\frac{1}{2}} \frac{\rho_G - \rho_i}{\xi \Delta x} - D_{i-\frac{1}{2}} \frac{\rho_i - \rho_{i-1}}{\Delta x}}{(1 + \xi) \Delta x}.$$

In this scheme, the ghost value, ρ_G , for ρ is provided by a quadratic extrapolation. Specifically, we construct a quadratic approximation, $\tilde{\rho}(x) = ax^2 + bx + c$, of ρ with $\tilde{\rho}(-\Delta x) = \rho_{i-1}$, $\tilde{\rho}(0) = \rho_i$, and $\tilde{\rho}(\xi \Delta x) = \rho_\Gamma$. Then, we define $\rho_G = \tilde{\rho}(\Delta x)$.

The linear systems resulting from the discretization of the adatom density, ρ , are solved by use of the combination of the biconjugate gradient stabilized iterative solver preconditioned with successive over-relaxation provided by the PETSc library. This computational approach is applied to the case with the Ehrlich–Schwoebel barrier and the case with irreversible aggregation.

Note that the quantity ρ_l is solved only for grid nodes that lie in the region Ω_l . To simplify subsequent calculations of the island boundary velocity, the values of ρ_l are extrapolated into a narrow band around the region Ω_l using the PDE-based approach of [30], so that valid values of ρ_l are available in some neighborhood of this region.

3.5. Motion of island boundaries

Next, we discuss the discrete scheme for updating the position of each island boundary. The normal velocity of the boundary of an island with height l is given by

$$\mathbf{v}_l = (D_{l-1} \nabla \rho_{l-1} \cdot \mathbf{n} - D_l \nabla \rho_l \cdot \mathbf{n}) \mathbf{n}.$$

In this equation D_l stands for diffusion coefficient on terrace height l and \mathbf{n} stands for normal direction to the island boundary pointing outwards.

Since the quantities ρ_l and ρ_{l-1} are available in some neighborhood of the island boundary (which is defined as the zero-level-set of ϕ_l), the gradients of ρ_l and ρ_{l-1} on the island boundary are obtained using standard finite-difference formulas. By the second-order accurate formula of Chen et al. [12], we have

$$\begin{aligned}\frac{\partial \rho}{\partial x} &= \frac{\rho_g - \rho_T}{s_g} \cdot \frac{s_5}{s_g + s_5} + \frac{\rho_T - \rho_5}{s_5} \cdot \frac{s_g}{s_g + s_5} - \frac{s_3 s_4 s_5}{2 s_g (s_5 + s_g)} \left(\frac{\rho_1 - \rho_T}{s_1} + \frac{\rho_2 - \rho_T}{s_2} \right) \cdot \frac{2}{s_2 + s_1}, \\ \frac{\partial \rho}{\partial y} &= \frac{\rho_1 - \rho_T}{s_1} \cdot \frac{s_2}{s_2 + s_1} + \frac{\rho_T - \rho_2}{s_2} \cdot \frac{s_1}{s_2 + s_1}.\end{aligned}$$

Once the velocity, \mathbf{v}_l , of each island boundary is computed, the level-set function, ϕ_l , is evolved according to equation (5). In this work, we use a semi-Lagrangian scheme, i.e. for any grid point \mathbf{x}^{n+1} , we write $\phi_l^{n+1}(\mathbf{x}^{n+1}) = \phi_l^n(\mathbf{x}_d)$ where \mathbf{x}_d is computed by

$$\begin{aligned}\hat{\mathbf{x}} &= \mathbf{x}^{n+1} - \frac{\Delta t}{2} \cdot \mathbf{v}_l^n(\mathbf{x}^{n+1}), \\ \mathbf{x}_d &= \mathbf{x}^{n+1} - \Delta t \cdot \mathbf{v}_l^{n+\frac{1}{2}}(\hat{\mathbf{x}}).\end{aligned}$$

The velocity field $\mathbf{v}_l^{n+\frac{1}{2}}$ at the mid-time step, $t^{n+\frac{1}{2}}$, is defined linearly from the previous velocity fields by $\mathbf{v}_l^{n+\frac{1}{2}} = \frac{3}{2} \mathbf{v}_l^n - \frac{1}{2} \mathbf{v}_l^{n-1}$. Finally, quantities at the locations \mathbf{x}_d and $\hat{\mathbf{x}}$ are approximated using non-oscillatory interpolation procedures; see [30] for details.

3.6. Transfer of data between grids

As the island boundaries evolve, the computational grid is automatically adapted so as to keep the smallest resolution near the boundary. Therefore, one needs to interpolate the data from the grid at time t^n to the grid at time t^{n+1} . Defining the data on a coarser grid from a finer one is trivial for a node-based approach since the values at the nodes of the coarser grid are simply those that existed on the finer grid. The reciprocal definition is carried out by the non-oscillatory quadratic interpolation scheme of [30]: for a unit cell $\mathcal{C} = [0, 1]^2$, the interpolated value of the adatom density, ρ , at the point (x, y) is

$$\begin{aligned}\rho(x, y) &= \rho(0, 0)(1-x)(1-y) \\ &\quad + \rho(0, 1)(1-x)(y) \\ &\quad + \rho(1, 0)(x)(1-y) \\ &\quad + \rho(1, 1)(x)(y) - \frac{\partial^2 \rho}{\partial x^2} \frac{x(1-x)}{2} - \frac{\partial^2 \rho}{\partial y^2} \frac{y(1-y)}{2},\end{aligned}\tag{12}$$

where

$$\frac{\partial^2 \rho}{\partial x^2} = \minmod_{v \in \text{vertices}(\mathcal{C})} (D_{xx}^0 \rho(v)) \quad \text{and} \quad \frac{\partial^2 \rho}{\partial y^2} = \minmod_{v \in \text{vertices}(\mathcal{C})} (D_{yy}^0 \rho(v)).$$

In the last two formulas, \minmod denotes the standard slope limiter operator [46,26]; and the second-order derivative, D_{xx}^0 , in the x -direction at node v_T is approximated with central differencing, viz.,¹

$$D_{xx}^0 \rho_T = \frac{\rho_G - \rho_T}{s_G} \cdot \frac{2}{s_1 + s_G} - \frac{\rho_T - \rho_1}{s_1} \cdot \frac{2}{s_1 + s_G}.$$

4. Numerical results

In this section we will present numerical results of our implementation of the IDM. In section 4.1 we will discuss how the parallelization and the adaptive mesh refinement affect the efficiency of our code. In section 4.2 we will present results that can be compared to previously published results obtained with a Dirichlet boundary condition to demonstrate that we do indeed include the same physical information as in previous work. Finally, in section 4.3 we show some initial results that illustrate how this approach allows us to efficiently reach growth regimes that were previously difficult or impossible to reach with existing approaches.

¹ The second-order derivative in the y -direction is approximated similarly.

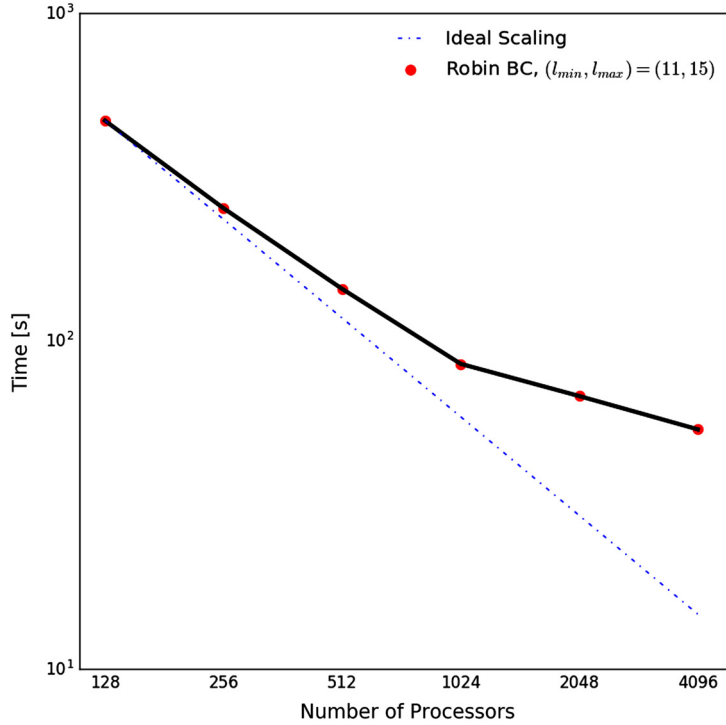


Fig. 12. Scaling of the computational time as a function of the number of processors. This scaling is performed on a lattice of size $L = 180$ on resolution levels (11, 15). The boundary condition is of Robin type with a barrier size of 0.2 and the final coverage is $\approx 0.9\%$ (i.e. 140 iterations in all cases).

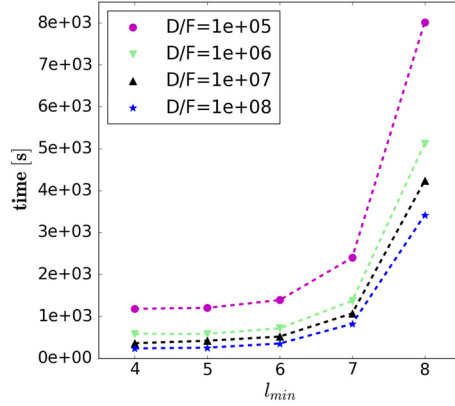


Fig. 13. Speedup from varying the adaptivity levels of the grid for different D/F values on a range of grid configurations. For all cases we use Robin boundary condition with a step edge barrier of size 0.2 and the final coverage is 20% covering only one layer (submonolayer growth). All simulations are run on a single processor.

4.1. Computational efficiency of the new approach

One of the key components of our revised approach and new implementation of the IDM is the parallelization of our code. The efficiency of this parallelization is shown in Fig. 12. Clearly, for the system size and parameters chosen for this example, we get almost perfect linear speedup of our code for using up to 1024 processors. We get very similar results for other simulations with different physical parameters. The speedup slows down (and eventually is reversed) when we use more than 1024 processors. The reason is that the extra cost associated with communication between processors becomes dominant compared to the amount of local computations. We have verified that this turning point in the scaling occurs when fewer (more) processors are used for systems with fewer (more) grid points in the simulations (data not shown).

The other major component of this approach is the adaptive mesh refinement using Quadtree grids. The efficiency of using adaptive grids and the speedup that can be achieved is shown in Fig. 13 for a maximum grid resolution of ($l_{\max} = 8$). Taking the coarsest grid resolution (i.e. the tree level l_{\min}) to be lower than the finest grid resolution (i.e. the tree level

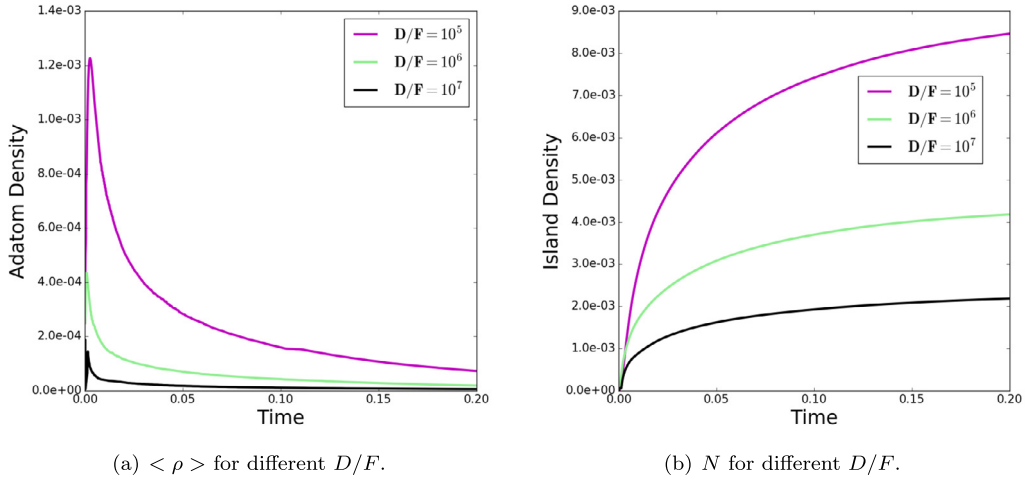


Fig. 14. The adatom density (left) and island density (right) for different values of D/F in the case of the boundary condition $\rho = 0$ (irreversible aggregation).

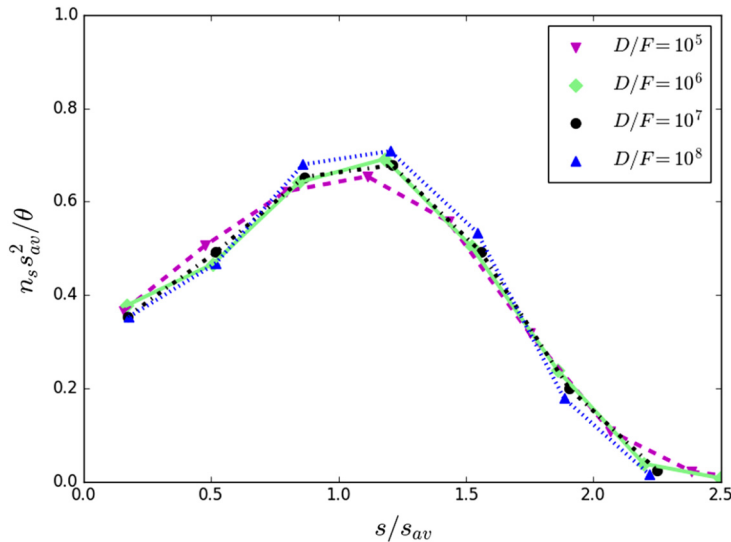


Fig. 15. Cluster size distribution in the case of the boundary condition $\rho = 0$ (irreversible aggregation). Each curve consists of 50 simulations with a lattice size of $L = 180$ on a 2×2 macro grid. Each simulation has a final coverage of 20%.

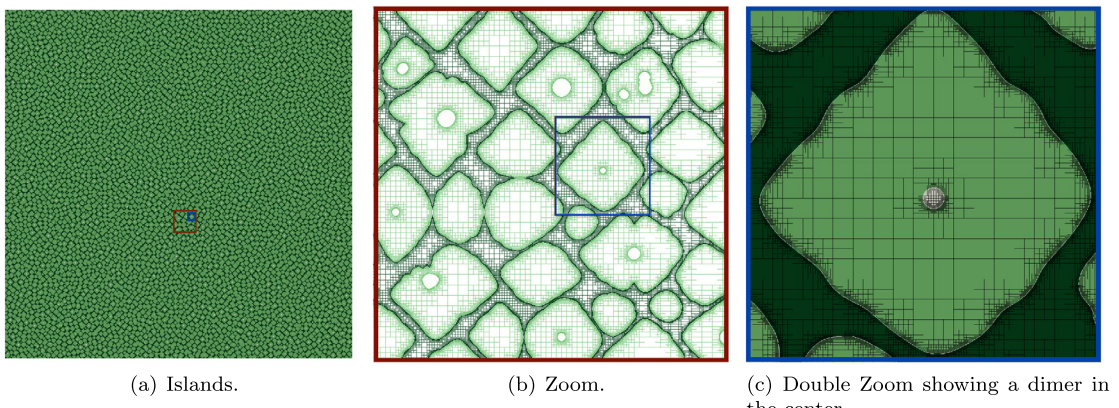


Fig. 16. The lattice has size $L = 1000$. Dirichlet boundary condition. This simulation uses a 2×2 macro grid with a (6, 13) Quadtree and 256 processors. The simulation took 48 hours.

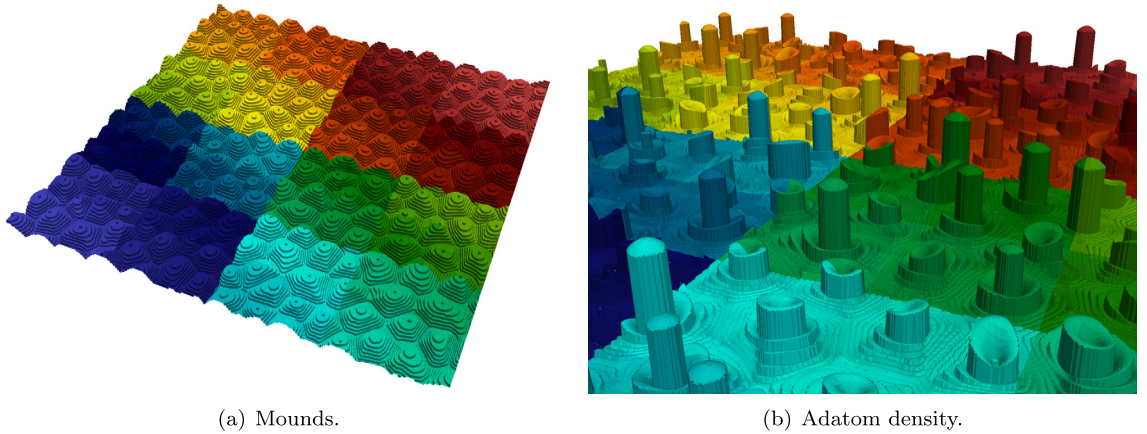


Fig. 17. Ehrlich–Schwoebel barrier and the formation of mounds in a deterministic seeding. The colors represent the processors' rank. This simulation uses a 2×2 macro grid with a (5, 9) Quadtree and took 24 hours on 192 processors with up to 1M nodes. The physical parameters are $L = 180$, $D/F = 10^5$ and $D'/D = 0.1$. 1,429 islands were nucleated, 7 layers grown with 93.0% coverage at the end, 40,000 time iterations.

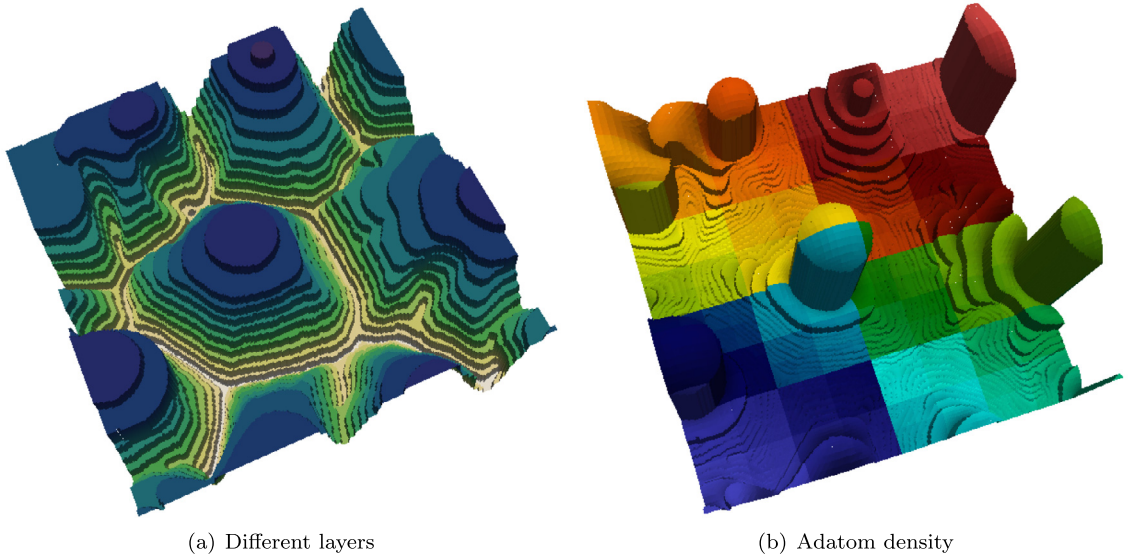


Fig. 18. Ehrlich–Schwoebel barrier and the formation of a single mound in a stochastic seeding. The lattice has size $L = 30$ and the $D/F = 10^5$. This simulation uses a 2×2 macro grid with a (5, 7) Quadtree and 256 processors. The left panel shows different layers (up to 11 layers) deposited and the right panel is a representation of the density field color coded by processor ranks. A closer look demonstrates the density is higher at the topmost layer of the island.

l_{\max}) leads to a significant reduction in the number of degrees of freedom, and thus in the computational cost by a factor of about 7 for (5, 8)-tree instead of a uniform (8, 8)-grid.

4.2. Results with the Dirichlet boundary condition for irreversible aggregation

We now discuss the validation of our implementation of the IMD, and focus on the case of irreversible aggregation, i.e. the case where $\rho = 0$ at the islands' boundary. For this case the IDM has been thoroughly validated against KMC simulations in [40]. We consider a lattice of size $L = 180^2$ and adaptive grids with levels (7, 11), on a 2×2 macro grid and $D/F = 10^5$, 10^6 , 10^7 and 10^8 . In the simulations discussed here the lattice size is chosen as $L = 180$ and the final coverage is 20%. Fig. 14 shows the adatom density and the island density as a function of coverage for different values of D/F . The results agree qualitatively and quantitatively with the results presented in [40].

In addition to densities we also check for the proper spatial distribution of the islands on the surface. The scaled island size distribution for the different values of D/F is shown in Fig. 15. These results also agree with the scaled island size distribution functions that were published in [40] (and that were validated against KMC simulations). Thus, we have checked that densities and morphologies that are obtained for irreversible aggregation (in the absence of a step edge barrier) are the ones that we expect for this model.

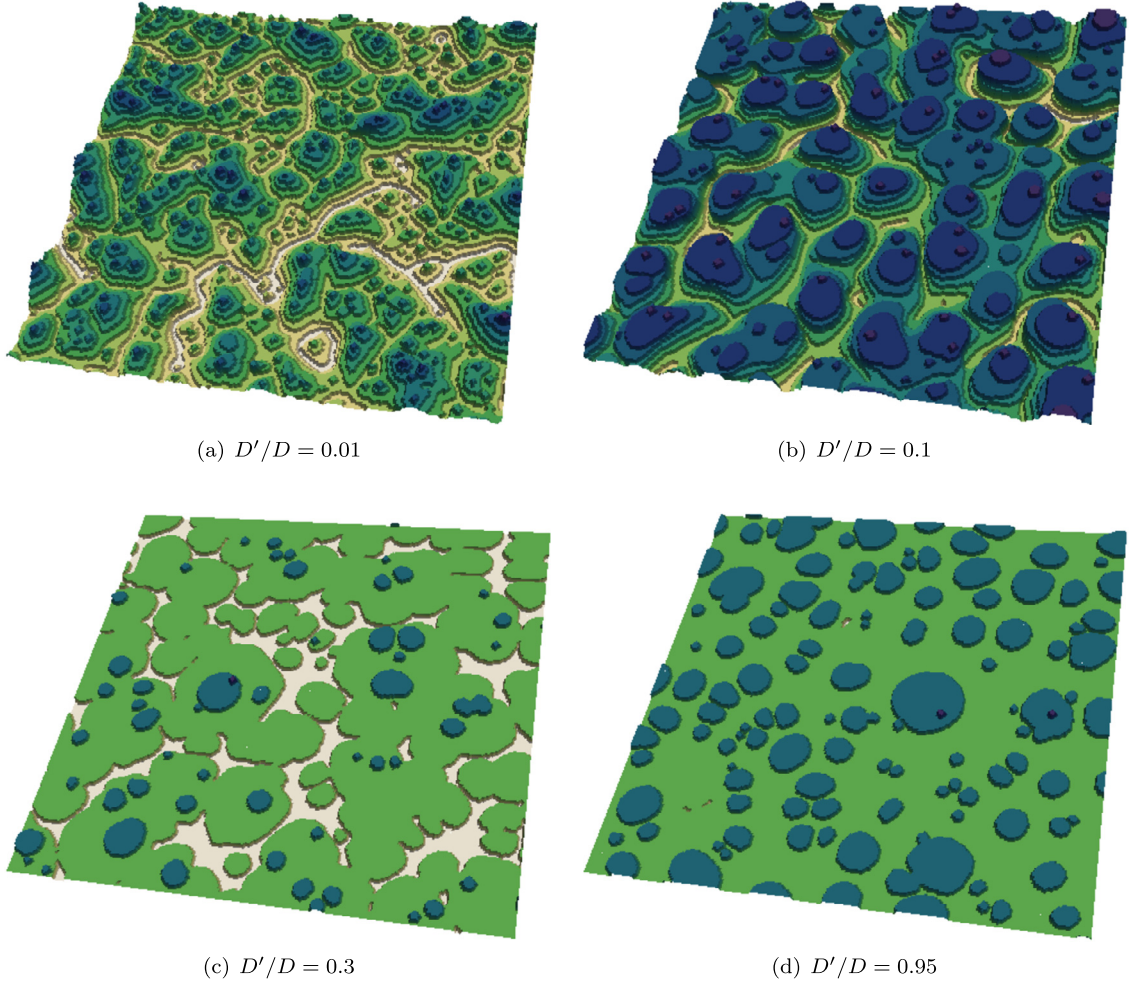


Fig. 19. Robin boundary condition and formation of mounds. The lattice has size $L = 180$ and the $D/F = 10^6$. This simulation uses a 2×2 macro grid with a (4, 7) Quadtree and 256 processors. The colors represent the islands heights with levels illustrated in each figure. All snapshots are at the same level.

Fig. 16 depicts the result of a simulation on a large lattice and with a high level of refinement. The zooms illustrate that small islands can be highly resolved, while at the same time large domains are considered. In particular, Fig. 16(c) shows that an island of size 2 is highly resolved.

4.3. Results with the Robin boundary condition to simulate the formation of mounds

We now turn our attention to simulations that use the Robin boundary condition that is needed to simulate the effect of an ES barrier. The results shown in Fig. 17(a) show the surface morphology and adatom density after the deposition of 7 layers for a simulation with an ES barrier defined by $D'/D = 0.1$ (i.e., for the case where an adatom at the edge of a terrace is 10 times more likely to stay on the terrace than it is to diffuse downward) and $D'' = 0.95D$. Clearly, even after just a few layers are grown we see the onset of mound formation. We note that these mounds are rather steep, and that in fact the typical terrace width in the middle of each side facet has a width that is of the order of one lattice constant (or even less). The reason that we do not see slope selection is that we do not include any mechanism for downward transport (such as downward funneling [22,3]). Nevertheless, close inspection of Fig. 17(b) illustrates that even for such small (narrow) terraces our adaptive scheme is able to resolve a meaningful adatom concentration on each terrace. For most mounds, the adatom concentration is rather low for lower layers (as these layers exhibit the most narrow terraces). The adatom concentration is larger for the topmost layer (or a few layers at the top), as these layers are not quite as narrow, and allow for a larger buildup of adatoms. This is better illustrated in Fig. 18 where a few mounds are formed.

Finally, Fig. 19 shows how the strength of the step edge barrier affects the formation of mounds. When $D'/D = 0.01$, we see clearly the formation of well defined mounds that are shaped like a “wedding cake” with 10 exposed terraces after the deposition of 11 layers. As D'/D increases (and the relative strength of the ES barrier weakens), mounds are less pronounced, and the morphology is very close to so-called layer-by-layer growth when $D'/D = 0.95$.

5. Conclusion

In this paper, we developed a computational method for simulating epitaxial growth on a forest of Octrees by use of the level set technique for the IDM. In our formulation, we considered both Dirichlet and Robin boundary conditions for the adatom density at the island boundaries. These boundary conditions correspond to the cases without a step edge barrier (Dirichlet condition) and with a step edge barrier (Robin condition). In addition, we described the implementation of a parallel framework for our code. Our simulation results are in qualitative and quantitative agreement with previously known results. This comparison offers a validation of our method in the physical context of the IDM.

One of the most significant aspects of our work is the fact that the efficiency of the implementation is orders of magnitude better than previous implementations of the IDM. Specifically, the parallel implementation of our code yields good scaling of the computational time versus the number of processors used; we have considered approximately 1000 processors and typical parameter choices. The Octree implementation allows us to use coarse grids away from islands that are much coarser than the fine grid near the boundaries. For some cases the coarse grid that we used was 128 coarser than the fine grid in each spatial direction, resulting in a large speedup without a noticeable decrease of accuracy.

This fast and efficient implementation allows us to study regimes of epitaxial growth that could not be reached in the past because of limitations of previous methods. We are currently working towards implementing the effect of ‘downward funneling’, a mechanism by which slope selection may occur in epitaxial growth. Our goal is to efficiently study the formation of mounds, and the selection of slopes as a competition between a step edge barrier and downward funneling. We also plan to implement the effect of step-step interactions, which is expected to compete with downward funneling for slope selection. Our ultimate, practical goal is to model and simulate the formation of quantum dots in the presence of strain on crystal surfaces.

Acknowledgements

The research of P. Mistani, D. Bochkov, A. Guittet and F. Gibou was supported by NSF DMS-1412695. The research of D. Margetis was supported by NSF DMS-1412769. The research of J. Schneider and C. Ratsch was supported by NSF DMS 1412392 and DMS 1440415. This work used the Extreme Science and Engineering Discovery Environment (XSEDE), which is supported by National Science Foundation grant number ACI-1053575. The authors acknowledge the Texas Advanced Computing Center (TACC) at The University of Texas at Austin for providing HPC and visualization resources that have contributed to the research results reported within this paper.

References

- [1] A. Voigt (Ed.), *Multiscale Modeling in Epitaxial Growth*, Birkhäuser Verlag, Basel, 2004.
- [2] G.S. Bales, D.C. Chrzan, Dynamics of irreversible island growth during submonolayer epitaxy, *Phys. Rev. B* 50 (1994) 6057–6067.
- [3] M.C. Bartelt, J.W. Evans, Transition to multilayer kinetic roughening for metal (100) homoepitaxy, *Phys. Rev. Lett.* 75 (Dec 1995) 4250–4253.
- [4] W. Barvosa-Carter, Private communication.
- [5] M. Bott, T. Michely, G. Comsa, The homoepitaxial growth of Pt on Pt(111) studied with STM, *Surf. Sci.* 272 (1992) 161–166.
- [6] C. Burstedde, L.C. Wilcox, O. Ghattas, p4est: scalable algorithms for parallel adaptive mesh refinement on forests of octrees, *SIAM J. Sci. Comput.* 33 (3) (2011) 1103–1133.
- [7] W.K. Burton, N. Cabrera, F.C. Frank, The growth of crystals and the equilibrium structure of their surfaces, *Philos. Trans. R. Soc. Lond. Ser. A* 243 (1951) 299–358.
- [8] R. Caflisch, M. Gyure, B. Merriman, S. Osher, C. Ratsch, D. Vvedensky, J. Zinck, Island dynamics and the level set method for epitaxial growth, *Appl. Math. Lett.* 12 (13) (1999).
- [9] R.E. Caflisch, Growth, structure and pattern formation for thin films, *J. Sci. Comput.* 37 (2008) 3–17.
- [10] R.E. Caflisch, M.F. Gyure, B. Merriman, C. Ratch, Kinetic model for a step edge in epitaxial growth, *Phys. Rev. E* 59 (1999) 6879–6887.
- [11] H. Chen, C. Min, F. Gibou, A second-order accurate FDM for the heat equation on irregular domains and adaptive grids, in: Proceedings of the Materials Research Society Symposium, San Francisco, CA, USA, vol. 910, 2006, pp. 907–910.
- [12] H. Chen, C. Min, F. Gibou, A supra-convergent finite difference scheme for the Poisson and heat equations on irregular domains and non-graded adaptive Cartesian grids, *J. Sci. Comput.* 31 (2007) 19–60.
- [13] H. Chen, C. Min, F. Gibou, A numerical scheme for the Stefan problem on adaptive Cartesian grids with supralinear convergence rate, *J. Comput. Phys.* 228 (16) (2009) 5803–5818.
- [14] S. Chen, M. Kang, B. Merriman, R. Caflisch, C. Ratsch, R. Fedkiw, M. Gyure, S. Osher, Level set method for thin film epitaxial growth, *J. Comput. Phys.* 167 (2001) 475.
- [15] A.A. Chernov, The spiral growth of crystals, *Sov. Phys. Usp.* 4 (1961) 116–148.
- [16] G. Ehrlich, F. Hudda, Atomic view of surface self-diffusion: tungsten on tungsten, *J. Chem. Phys.* 44 (1966) 1039.
- [17] H.-J. Ernst, F. Fabre, R. Folkerts, J. Lapujoulade, Observation of a growth instability during low temperature molecular beam epitaxy, *Phys. Rev. Lett.* 72 (1994) 112–115.
- [18] F. Gibou, R. Fedkiw, L.-T. Cheng, M. Kang, A second-order accurate symmetric discretization of the Poisson equation on irregular domains, *J. Comput. Phys.* 176 (2002) 205–227.
- [19] F. Gibou, C. Ratsch, R. Caflisch, Capture numbers in rate equations and scaling laws for epitaxial growth, *Phys. Rev. B* 67 (2003) 155403.
- [20] F. Gibou, C. Ratsch, S. Chen, M. Gyure, R. Caflisch, Rate equations and capture numbers with implicit island correlations, *Phys. Rev. B* 63 (2001) 1154.
- [21] A. Helgadóttir, F. Gibou, A Poisson–Boltzmann solver on irregular domains with Neumann or Robin boundary conditions on non-graded adaptive grid, *J. Comput. Phys.* 230 (2011) 3830–3848.
- [22] P. Šmilauer, D.D. Vvedensky, Coarsening and slope evolution during unstable epitaxial growth, *Phys. Rev. B* 52 (1995) 14263–14272.
- [23] H.-C. Jeong, E.D. Williams, Steps on surfaces: experiment and theory, *Surf. Sci. Rep.* 34 (1999) 171–294.
- [24] J. Krug, P. Politi, T. Michely, Island nucleation in the presence of step-edge barriers: theory and applications, *Phys. Rev. B* 61 (2000) 14037.

- [25] J. Langer, Instability and pattern formation in crystal growth, *Rev. Mod. Phys.* 52 (1980) 1–28.
- [26] X.-D. Liu, S. Osher, T. Chan, Weighted essentially non-oscillatory schemes, *J. Comput. Phys.* 126 (1996) 202–212.
- [27] J. Lu, J.-G. Liu, D. Margetis, Emergence of step flow from an atomistic scheme of epitaxial growth in 1 + 1 dimensions, *Phys. Rev. E* 91 (2015) 032403.
- [28] T. Michely, J. Krug, Islands, Mounds and Atoms: Patterns and Processes in Crystal Growth Far from Equilibrium, Springer-Verlag, 2004.
- [29] C. Min, F. Gibou, Geometric integration over irregular domains with application to level-set methods, *J. Comput. Phys.* 226 (2007) 1432–1443.
- [30] C. Min, F. Gibou, A second order accurate level set method on non-graded adaptive Cartesian grids, *J. Comput. Phys.* 225 (1) (2007) 300–321.
- [31] C. Min, F. Gibou, H. Ceniceros, A supra-convergent finite difference scheme for the variable coefficient Poisson equation on non-graded grids, *J. Comput. Phys.* 218 (2006) 123–140.
- [32] M. Mirzadeh, A. Guittet, C. Burstedde, F. Gibou, Parallel level-set methods on adaptive tree-based grids, *J. Comput. Phys.* 322 (2016) 345–364.
- [33] X. Niu, R. Vardavas, R. Caflisch, C. Ratsch, A level set simulation of directed self-assembly during epitaxial growth, *Phys. Rev. B* 74 (2006) 193403.
- [34] S. Osher, J.A. Sethian, Fronts propagating with curvature dependent speed: algorithms based on Hamilton–Jacobi formulations, *J. Comput. Phys.* 79 (1) (1988) 12–49.
- [35] J. Papac, F. Gibou, C. Ratsch, Efficient symmetric discretization for the Poisson, heat and Stefan-type problems with Robin boundary conditions, *J. Comput. Phys.* 229 (2010) 875–889.
- [36] J. Papac, A. Helgadottir, C. Ratsch, F. Gibou, A level set approach for diffusion and Stefan-type problems with Robin boundary conditions on quadtree/octree adaptive Cartesian grids, *J. Comput. Phys.* 233 (2013) 241–261.
- [37] S. Paulin, F. Gillet, O. Pierre-Louis, C. Misbah, Unstable step meandering with elastic interactions, *Phys. Rev. Lett.* 86 (2001) 5538–5541.
- [38] A. Pimpinelli, J. Villain, Physics of Crystal Growth, Cambridge University Press, Cambridge, UK, 1999.
- [39] C. Ratsch, M. Gyure, S. Chen, M. Kang, D. Vvedensky, Fluctuation and scaling in aggregation phenomena, *Phys. Rev. B* 61 (2000) R10598.
- [40] C. Ratsch, M.F. Gyure, R.E. Caflisch, F. Gibou, M. Petersen, M. Kang, J. Garcia, D.D. Vvedensky, Level-set method for island dynamics in epitaxial growth, *Phys. Rev. B* 65 (2002) 195403.
- [41] G. Russo, P. Smereka, A remark on computing distance functions, *J. Comput. Phys.* 163 (2000) 51–67.
- [42] H. Samet, The Design and Analysis of Spatial Data Structures, Addison-Wesley, New York, 1989.
- [43] H. Samet, Applications of Spatial Data Structures: Computer Graphics, Image Processing and GIS, Addison-Wesley, New York, 1990.
- [44] R.L. Schwoebel, E.J. Shipsey, Step motion on crystal surfaces, *J. Appl. Phys.* 37 (1966) 3682–3686.
- [45] G.H. Shortley, R. Weller, Numerical solution of Laplace's equation, *J. Appl. Phys.* 9 (1938) 334–348.
- [46] C.-W. Shu, S. Osher, Efficient implementation of essentially non-oscillatory shock capturing schemes II, *J. Comput. Phys.* 83 (1989) 32–78.
- [47] J.A. Stroscio, D.T. Pierce, M.D. Stiles, A. Zangwill, L.M. Sander, Coarsening of unstable surface features during Fe(001) homoepitaxy, *Phys. Rev. Lett.* 75 (1995) 4246–4249.
- [48] M. Sussman, P. Smereka, S. Osher, A level set approach for computing solutions to incompressible two-phase flow, *J. Comput. Phys.* 114 (1994) 146–159.
- [49] D. Vanderbilt, L.K. Wickham, Evolution of thin film and surface microstructure, in: J.Y.T. Thompson, D.J. Srolovitz (Eds.), MRS, Pittsburgh, 1991, p. 155.
- [50] J. Villain, Continuum models of crystal growth from atomic beams with and without desorption, *J. Phys. (France)* I 1 (1991) 19–42.
- [51] P. Šmilauer, D.D. Vvedensky, Coarsening and slope evolution during unstable epitaxial growth, *Phys. Rev. B* 52 (1995) 14263–14272.
- [52] D. Vvedensky, C. Ratsch, F. Gibou, R. Vardavas, Singularities and spatial fluctuations in submonolayer epitaxy, *Phys. Rev. Lett.* 90 (2003) 189601.
- [53] J. Wollschläger, E.Z. Luo, M. Henzler, Diffraction characterization of rough films formed under stable and unstable growth conditions, *Phys. Rev. B* 57 (1998) 15541–15552.
- [54] A.D. Yoffe, Low-dimensional systems: quantum size effects and electronic properties of semiconductor microcrystallites (zero-dimensional systems) and some quasi-two-dimensional systems, *Adv. Phys.* 42 (1993) 173–262.
- [55] J.-K. Zuo, J.F. Wendelken, Evolution of mound morphology in reversible homoepitaxy on Cu(100), *Phys. Rev. Lett.* 78 (1997) 2791–2794.